



Photocorrosion inhibition and high-efficiency photoactivity of porous $\text{g-C}_3\text{N}_4/\text{Ag}_2\text{CrO}_4$ composites by simple microemulsion-assisted co-precipitation method

Yanyang Shang, Xi Chen, Wenwen Liu, Pengfei Tan, Haoyun Chen, Laidi Wu, Cheng Ma, Xiang Xiong, Jun Pan*

State Key Laboratory for Powder Metallurgy, Central South University, Changsha, 410083, China

ARTICLE INFO

Article history:

Received 21 April 2016

Received in revised form

10 November 2016

Accepted 15 November 2016

Available online 16 November 2016

Keywords:

$\text{g-C}_3\text{N}_4$

Ag_2CrO_4

Porous $\text{g-C}_3\text{N}_4/\text{Ag}_2\text{CrO}_4$ composites

Visible-light photocatalysis

Photocorrosion inhibition

ABSTRACT

A facile microemulsion-assisted co-precipitation method was carried out to synthesize nano-sized Ag_2CrO_4 highly dispersed on the surface of porous $\text{g-C}_3\text{N}_4$ as high-efficiency visible-light-driven composite photocatalysts for the first time. The structure and morphology of the composites were systematically characterized by various techniques. Compared with Ag_2CrO_4 and $\text{g-C}_3\text{N}_4$, $\text{g-C}_3\text{N}_4/\text{Ag}_2\text{CrO}_4$ composites showed a dramatically increased photocatalytic activity in degradation of rhodamine B (RhB) and methylene blue (MB). The optimum mass ratio of the Ag_2CrO_4 to $\text{g-C}_3\text{N}_4$ was about 30 wt%, the degradation rate of which were 6.1 (7.9) and 9.7 (15.2) times higher than pure Ag_2CrO_4 and $\text{g-C}_3\text{N}_4$ in RhB (MB) degradation, respectively. The excellent photocatalytic activity and stability mainly benefited from the synergistic effect including smaller Ag_2CrO_4 particle size, high specific surface area of the composites and matched band potentials which not only promoted the separation of photon-generated charge carriers, but also inhibited the photocorrosion of Ag_2CrO_4 . Further study revealed that the photocatalytic mechanism followed a Z-scheme which provided an efficient transfer pathway for charge carriers meanwhile endowed the composites with strong oxidation and reduction ability. Hence the porous $\text{g-C}_3\text{N}_4/\text{Ag}_2\text{CrO}_4$ composites are potential in environmental purification.

© 2016 Elsevier B.V. All rights reserved.

1. Introduction

Since Fujishima and Honda found photoinduced water splitting over a TiO_2 electrode [1], semiconductor photocatalysis technology has attracted tremendous attention owing to its potential in environmental remediation [2–4]. Despite its superior performance, TiO_2 is limited in applications for intrinsically wide band gap (3.2 eV) makes it can only absorb ultraviolet (UV) light [5–7]. Therefore, much effort has been devoted to investigating and preparing highly efficient visible-light-driven photocatalysts [8–11].

Recently, a variety of Ag-based semiconductor photocatalysts have been capturing considerable attention because of their outstanding photocatalytic performance in decomposition of organic pollutants, water splitting and CO_2 reduction [12–14]. Among them, Ag_2CrO_4 is gaining increasing concern due to its narrow band gap (1.75 eV), unique crystal structure and electronic structure [15,16]. Both theoretical calculation and experiments have proved

that Ag_2CrO_4 possessed high photocatalytic activity owing to its strong optical absorption coefficient and high oxidization ability of photo-generated holes [17–20]. Unfortunately, photocorrosion is the fatal drawback of Ag_2CrO_4 which will seriously damage its structure and thus deteriorate the photocatalytic activity [20,21]. Therefore, an urgent task is to keep the photo-generated electrons away from Ag_2CrO_4 before reducing the Ag^+ to Ag^0 and recombining with holes. Just like other coupled systems such as CdS/GO [22], ZnO/ZnS [23] and $\text{Ag}_3\text{PO}_4/\text{TiO}_2$ [24], coupling Ag_2CrO_4 with stable and band structure matching semiconductors seems a sensible way to address the issue of photocorrosion.

Graphitic carbon nitride ($\text{g-C}_3\text{N}_4$) with a moderate band gap (2.7 eV) has been extensively studied in recent years owing to its outstanding photocatalytic performance and physicochemistry stability [25,26]. Since $\text{g-C}_3\text{N}_4$ is a favorable substrate can act as both electron donor and acceptor [27], much work has been done to hybridize $\text{g-C}_3\text{N}_4$ with other semiconductors for further enhancing the photocatalytic activity [28]. Noticeably, by coupling $\text{g-C}_3\text{N}_4$ with Ag_3PO_4 , photo-generated electrons of Ag_3PO_4 could flow to $\text{g-C}_3\text{N}_4$ much easier and faster, avoiding the aggregation of electrons and then suppressing the photocorrosion of Ag_3PO_4 [13,27]. Simul-

* Corresponding author.

E-mail address: jun.pan@csu.edu.cn (J. Pan).

taneously, rapid transfer and separation of photo-generated charge carriers lead to a dramatically enhanced photocatalytic activity. Inspired by the foregoing discussion, it seems feasible to construct g-C₃N₄/Ag₂CrO₄ composite as a robust photocatalyst for stabilizing Ag₂CrO₄ and greatly improving the visible-light photoactivity.

It is known that the activity of photocatalyst heavily depends on its structure and morphology which are normally decided by the synthetic methods. In traditional precipitation methods, the particles size is relatively large, particles are easily agglomerated and show a nonuniform size distribution [29,30]. Microemulsion, as an isotropic and thermodynamic stable system, has been widely applied in fabrication of monodispersed and morphology-controlled nano-sized particles which could shorten the diffusion process of photo-generated excitons and increase the utilization of light [31,32]. Moreover, co-precipitation has been employed as an effective method to fabricate g-C₃N₄-composited photocatalysts in many reported literatures [12,13,27]. In contrast with bulk g-C₃N₄, porous g-C₃N₄ with high specific surface area and abundant micropores provides more active sites and attachment points for nanoparticles, which is much suitable to form composite photocatalysts.

Herein, combining the advantages of the microemulsion and co-precipitation methods, we constructed a porous g-C₃N₄/Ag₂CrO₄ composite photocatalysts via a facile microemulsion-assisted co-precipitation method for the first time. The composites exhibited fascinating photocatalytic activity and recyclability on degradation of organic dyes. The enhanced photoactivity and stability were mainly ascribed to the synergistic effect between Ag₂CrO₄ and g-C₃N₄. Further experimental results demonstrated that the reaction mechanism followed a Z-scheme which possessed highly efficient separation of photo-generated charge carriers and a strong redox ability [33,34]. Notably, the photocorrosion of Ag₂CrO₄ was significantly inhibited since g-C₃N₄ served as an electron transfer media and acceptor.

2. Experimental section

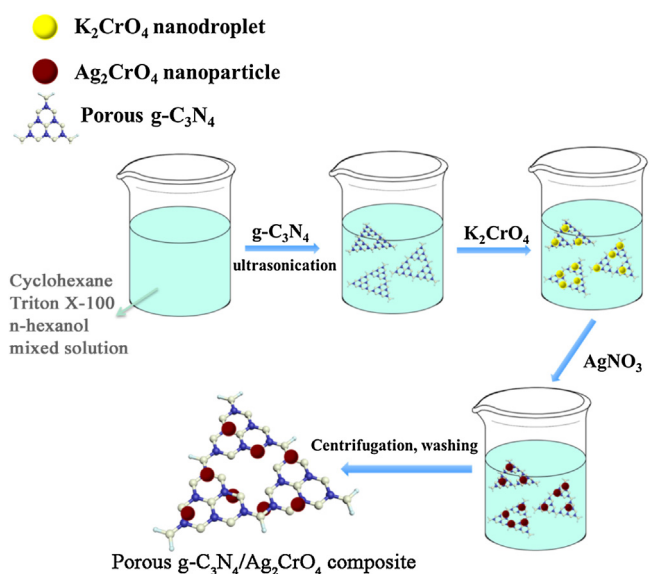
2.1. Chemicals

Urea (Aladdin AR 99%), silver nitrate (Aladdin AR 99%), potassium chromate (Aladdin AR 99%), cyclohexane (Sinopharm Chemical Reagent AR), n-hexanol (Sinopharm Chemical Reagent AR), Triton X-100 (Sinopharm Chemical Reagent AR), rhodamine B (Aladdin AR), methylene blue aqueous solution (Aladdin 0.05 wt%), indium tin glass (Kaivo Optoelectronic), Nafion (Sigma 5 wt%), Ethylenediamine tetraacetic acid disodium salt (Sinopharm Chemical Reagent AR), p-benzoquinone (Aladdin 99%), *tert*-butyl alcohol (Aladdin AR 99%). All other reagents used in this study were analytically pure grade and without further purification.

2.2. Synthesis of porous g-C₃N₄/Ag₂CrO₄ composites

The porous g-C₃N₄ was prepared through direct heating of urea in a ceramic crucible with a cover in air. In a typical process, 8 g urea was put into a crucible and the crucible was heating at 500 °C for 4 h in a muffle furnace with a heating rate of 2.3 °C/min. After calcination, the obtained porous g-C₃N₄ was washed and collected for further usage.

Porous g-C₃N₄/Ag₂CrO₄ composites were synthesized according to the following process: as illustrated in Scheme 1, 32 mL cyclohexane (oil phase), 10 mL Triton X-100 (surfactant), and 8 mL n-hexanol (co-surfactant) were mixed via magnetic stirring. After stirring, 100 mg g-C₃N₄ was added into the above clear solution and ultrasonication 30 min to form a homogeneous suspension. Then, a certain amount of K₂CrO₄ aqueous solution (0.25 M) was added into



Scheme 1. Schematic representation of porous g-C₃N₄/Ag₂CrO₄ composites synthesized by microemulsion-assisted co-precipitation method.

the suspension drop by drop to achieve a W/O reversed-micellar system, followed by vigorously stirring for 1 h to make the CrO₄²⁻-contained water droplets adsorb on the surface of hydrophilic g-C₃N₄. Subsequently, the stoichiometric AgNO₃ aqueous solution (0.5 M) was dripped into above suspension after which stirring for another 1 h. The resultant suspension was aged for 6 h. The precipitate was collected by centrifugation then washed by deionized (DI) water and ethanol for three times. The final products were obtained by drying at 60 °C in air dry oven. Through this method, porous g-C₃N₄/Ag₂CrO₄ composites with different mass ratios of Ag₂CrO₄ to g-C₃N₄ were synthesized. The theoretical mass ratios of Ag₂CrO₄ to g-C₃N₄ were 0.2, 0.3, 0.4 and 0.6, and were named as ACO/CN-0.2, ACO/CN-0.3, ACO/CN-0.4, ACO/CN-0.6, respectively. For comparison, pure Ag₂CrO₄ was synthesized in the similar procedure without addition of g-C₃N₄. The whole experimental process was operated in dark as possible.

2.3. Characterization

The crystal structure of samples were obtained by X-ray diffraction (XRD; D/max 2550, Rigaku Corporation) with Cu K α radiation ($\lambda = 0.15405$ nm). The XRD patterns were recorded in the diffraction angle (2θ) ranging from 10 to 70° at a scan rate of 10°/min. Fourier transform infrared spectra (FTIR) were measured on an infrared spectroscope (Nicolet 6700, Thermo Nicolet Corporation) in the range of 4000–500 cm⁻¹, using KBr pellets as reference. Surface chemical states were analyzed by X-ray photoelectron spectroscopy (ESCALAB 250Xi, ThermoFisher-VG Scientific), and the binding energies of all the elements were calibrated through the C 1s peak (BE = 284.8 eV) as standard. Morphologies were observed on a scanning electron microscope (Nova Nano SEM 230, FEI Co., Ltd.) with an acceleration voltage of 10 KV and a field emission transmission electron microscope (FETEM, JEM-2100F, Japanese electronics Co., Ltd.) with an acceleration voltage of 200 KV. Specific surface areas were determined by a nitrogen adsorption instrument (Quadasorb SI-3MP) at 77 K after degassed at 180 °C for 6 h. The pore size distributions were determined using the Barrett-Joyner-Halenda (BJH) method. The UV-vis diffuse reflectance spectra of the catalysts were recorded on a UV-vis spectrometer (Evolution 220, Thermo Fisher Scientific) in the range of 300 to 1100 nm, at a scan rate of 200 nm/min, using BaSO₄ as reference. Photoluminescence

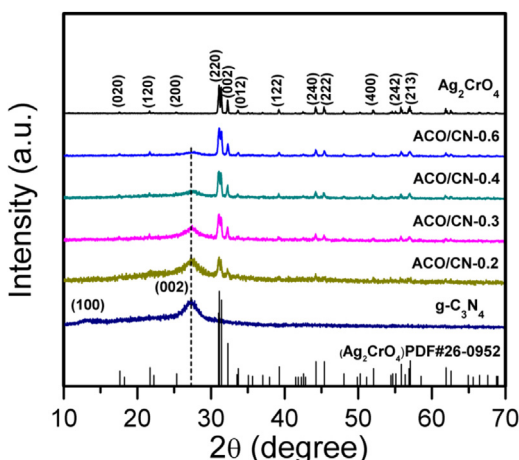


Fig. 1. XRD patterns of Ag_2CrO_4 , $\text{g-C}_3\text{N}_4$, and $\text{g-C}_3\text{N}_4/\text{Ag}_2\text{CrO}_4$ composites.

spectra (PL) of the catalysts were carried out on a spectrophotometer (F-4600, Hitachi, Ltd.) under the excitation wavelength of 370 nm produced by a He-Cd laser.

2.4. Photocatalytic activity evaluation

The photocatalytic activities of all the as-prepared samples were evaluated by degradation of RhB and MB in aqueous solution under visible light irradiation ($\lambda \geq 420$ nm). The visible light was produced by a 300 W Xe lamp with a 420 nm cut-off filter. In each experiment, 10 mg photocatalyst was put into a quartz tube with 15 mL RhB (MB) aqueous solution (10 mg/L) to form a homogeneous suspension. Before reaction, the suspension was magnetically stirred for 1 h in the dark to reach adsorption-desorption equilibrium between the catalysts and the dyes. Then the quartz tube was exposed to the visible light under magnetically stirring with a 15 min interval. During each interval, 5 mL suspension was taken out, centrifuged to remove the insoluble particles and the cleaned solution was analyzed by a UV-vis spectrophotometer. The concentrations of RhB and MB were determined as a function of irradiation time by recording the absorbance located in 554 and 664 nm, respectively. The similar procedure was used in the active species trapping experiments, except that different scavengers were added.

2.5. Photoelectrochemistry measurement

The electrochemical impedance spectra (EIS) of the photocatalysts were obtained using an electrochemical workstation (CHI 660e, China). A standard three-electrode system was performed in this photochemical study. The platinum plate was employed as a counter electrode and a standard calomel electrode as a reference electrode, 0.1 M sodium sulfate aqueous solution as electrolyte. The working electrodes were manufactured as follows: 12 mg photocatalysts were dispersed in 500 μL ethanol with 20 μL 5 wt% Nafion aqueous solution. Then, 60 μL above suspension was dropped onto the surface of 1 cm \times 1 cm indium tin oxide (ITO) glass. Subsequently, the ITO coated with photocatalysts annealed for 2 h in air at 200 °C. The EIS was implemented at 5 mV amplitude and frequency range of 1000 KHz to 0.1 Hz.

3. Results and discussion

3.1. Characterizations of as-prepared photocatalysts

XRD patterns of all as-prepared samples were shown in Fig. 1. For pure $\text{g-C}_3\text{N}_4$, two typical peaks at about 13.2° and 27.4° were

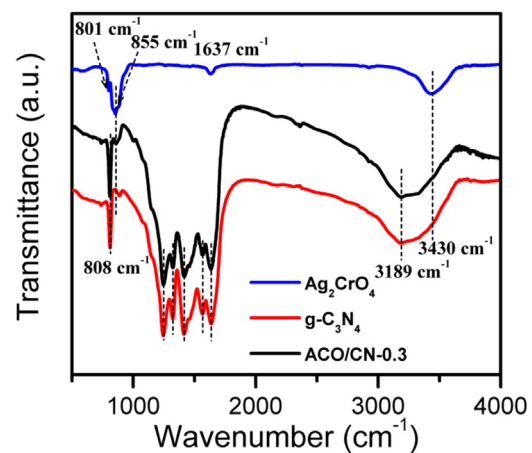


Fig. 2. FT-IR spectra of Ag_2CrO_4 , $\text{g-C}_3\text{N}_4$, and ACO/CN-0.3.

corresponding to (110) and (002) diffraction plane, ascribed to the repeating arrangement of the tri-s-triazine rings and the stacking of the conjugated aromatic systems, respectively. Pure Ag_2CrO_4 showed a high crystallinity and the appeared diffraction peaks originated from its orthorhombic structure (JCPDS No. 26-0952). For $\text{g-C}_3\text{N}_4/\text{Ag}_2\text{CrO}_4$ composites, all the diffraction peaks could be attributed to the Ag_2CrO_4 and $\text{g-C}_3\text{N}_4$ and the peak intensities of $\text{g-C}_3\text{N}_4$ decreased with the decrease of $\text{g-C}_3\text{N}_4$ content. Moreover, the (110) peak of $\text{g-C}_3\text{N}_4$ almost disappeared in the composites mainly due to the low crystallinity of $\text{g-C}_3\text{N}_4$. No impurity can be observed in the XRD patterns.

The FTIR spectra of pure Ag_2CrO_4 , $\text{g-C}_3\text{N}_4$ and $\text{g-C}_3\text{N}_4/\text{Ag}_2\text{CrO}_4$ composites were shown in Fig. 2. ACO/CN-0.3 was used to represent the composite photocatalysts in this article. Of all the spectra, the broad peaks appeared at 3430 and 1637 cm^{-1} are indicative of hydroxyl groups stretching vibration caused by the absorption of hydrated oxide. For pure $\text{g-C}_3\text{N}_4$, the peak at 3189 cm^{-1} belong to N-H stretching vibration, whereas peaks in the range of 1200–1650 cm^{-1} were related to the C=N and C≡N stretching vibration mode [35], besides, the peak at 808 cm^{-1} came from s-triazine ring vibrations. In the case of Ag_2CrO_4 , the peak at 855 cm^{-1} with a shorter at about 801 cm^{-1} could be ascribed to the stretching vibration of the Cr-O bond in CrO_4 tetrahedra [29,36]. All the characteristic absorption peaks of $\text{g-C}_3\text{N}_4$ and Ag_2CrO_4 were observed in the ACO/CN-0.3, revealing that Ag_2CrO_4 successfully composited with $\text{g-C}_3\text{N}_4$, which was consistent with XRD results.

XPS spectra were carried out to further investigate the surface chemical state and bonding configuration of the as-prepared photocatalysts. As shown in Fig. 3. In the survey spectra, all signals of C, N, Ag, Cr, O elements were detected in the ACO/CN-0.3 composite, suggesting its hybrid structure which was in accord with the XRD and FTIR results. Form the high resolution X-ray photoelectron spectra (HRXPS) of C 1s shown in Fig. 3b, only one peak at 284.8 eV could be observed in pure Ag_2CrO_4 which was related to adsorptive adventitious hydrocarbon, while for $\text{g-C}_3\text{N}_4$ and ACO/CN-0.3, C 1s peak were divided into three peaks. The other two peaks at around 286.1 and 288.3 eV were attributed to sp²-bonded in s-triazine rings (N=C=N) and combination of C=N groups in $\text{g-C}_3\text{N}_4$, respectively. In the N 1s HRXPS spectra of $\text{g-C}_3\text{N}_4$ and ACO/CN-0.3, three apparent peaks at around 398.8, 400.1, and 401.3 eV were corresponding to sp²-bonded nitrogen atoms (N=C=N), tertiary nitrogen (N-(C)₃) and N-H side groups, respectively. An un conspicuous peak appeared at 404.6 eV originated from the charge effect [37]. Fig. 3d showed the O 1s HRXPS spectra split into two peaks at around 530.0 and 531.6 eV, the former was derived from crystal lattice oxygen of Ag_2CrO_4 and the latter come from the chemisorbed oxygen of surface hydroxyls [38]. Notably, comparing with primi-

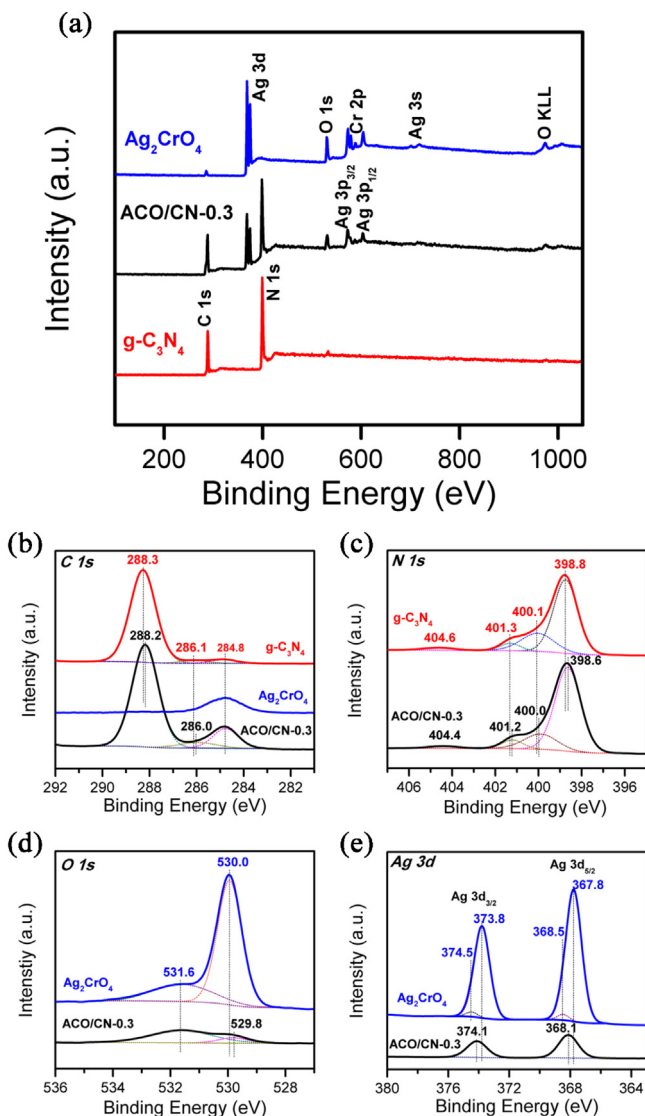


Fig. 3. XPS spectra of Ag_2CrO_4 , $\text{g-C}_3\text{N}_4$, and ACO/CN-0.3 : (a) survey spectra, (b) high resolution C 1s, (c) high resolution N 1s, (d) high resolution O 1s and (e) high resolution Ag 3d.

tive $\text{g-C}_3\text{N}_4$ and Ag_2CrO_4 , binding energy of C 1s, N 1s and O 1s were all slightly decreased for ACO/CN-0.3 . The shift of binding energy was also observed in many other $\text{g-C}_3\text{N}_4$ -based composites system, which indicated that there were some interactions between Ag_2CrO_4 and $\text{g-C}_3\text{N}_4$ [37,39]. As illustrated in Fig. 3e, the peaks at 367.8, 373.8 and 368.1, 374.1 eV were assigned to Ag^+ of Ag_2CrO_4 and ACO/CN-0.3 , respectively. Where those at 368.5 and 374.5 eV were related to Ag^0 of Ag_2CrO_4 , the generated trace amounts of Ag^0 during preparation process mainly implied the photosensitivity of Ag_2CrO_4 [17]. Interestingly, the binding energy of Ag^+ for ACO/CN-0.3 is higher than pure Ag_2CrO_4 , which was much different from other elements. The blue shift of Ag^+ peak probably revealed that an increased electron density in Ag^+ , indicating the existence of electron transfer between Ag_2CrO_4 and $\text{g-C}_3\text{N}_4$ nanosheets upon hybridization [40]. This phenomenon further confirmed that the interactions were existed in the hybrid structure, which might be conducive to migration of photo-generated charge carriers and thus enhanced the photocatalytic performance.

SEM was carried out to observe the morphologies of as-prepared photocatalysts. Fig. 4 showed the typical SEM images of pure Ag_2CrO_4 (a), porous $\text{g-C}_3\text{N}_4$ (b) and porous $\text{g-C}_3\text{N}_4/\text{Ag}_2\text{CrO}_4$ com-

posites with different mass ratio (c-f). It was clearly seen that Ag_2CrO_4 nanoparticles were seriously aggregated, primitive $\text{g-C}_3\text{N}_4$ exhibited a plicated and smooth surface with some irregular mesopores. After hybrid, Ag_2CrO_4 nanoparticles were loaded on the surface of $\text{g-C}_3\text{N}_4$ with a homogeneous distribution. Moreover, the agglomeration of Ag_2CrO_4 was significantly alleviated with its mass ratio decreased.

Morphologies and microstructures of the samples were obtained by TEM and HRTEM. As illustrated in Fig. 5, Ag_2CrO_4 particles were severely aggregated, its particle size ranged between 50 nm and 100 nm with an inhomogeneity distribution. A number of mesopores in $\text{g-C}_3\text{N}_4$ could be much clearly seen in Fig. 5b, furthermore, the porous $\text{g-C}_3\text{N}_4$ was relatively transparent under transmission electron beam, which indicated its thin nature. Ag_2CrO_4 nanoparticles uniformly dispersed on the surface of $\text{g-C}_3\text{N}_4$ and the particle size was about 30 nm which was much smaller than pure Ag_2CrO_4 . This phenomenon might be interpreted as follows: in the microemulsion system, K_2CrO_4 aqueous solution was evenly dispersed in oil phase and restricted into nano-sized droplets, the nano-sized droplets would adsorb on the surface of $\text{g-C}_3\text{N}_4$ because the exposed amino groups in $\text{g-C}_3\text{N}_4$ made it possess a good hydrophilicity. The droplets served as a nanoreactor and the $\text{g-C}_3\text{N}_4$ could provide nucleation sites for Ag_2CrO_4 growth. After the addition of AgNO_3 , generated Ag_2CrO_4 could be anchored onto the surface of $\text{g-C}_3\text{N}_4$, thus hindering the agglomeration and growth of the particles [31,41,42]. The smaller particle size of Ag_2CrO_4 enlarged the interface contact area with $\text{g-C}_3\text{N}_4$, which was conducive to enhancing the photocatalytic activity. In HRTEM image of ACO/CN-0.3 , clear lattice fringe was observed, corresponding to the (240) planes of Ag_2CrO_4 with an interplanar spacing of 0.204 nm. Lattice fringe of $\text{g-C}_3\text{N}_4$ was difficult to see because of its low crystallinity and weak two-dimensional ordering [43]. Besides, a close contact interface was also observed in HRTEM, which could benefit the separation of photo-generated charge carriers.

The specific surface areas and pore size distributions of Ag_2CrO_4 , $\text{g-C}_3\text{N}_4$ and ACO/CN-0.3 were determined by nitrogen adsorption-desorption isotherm analysis. Fig. 6 presented the type IV isotherms with a hysteresis loop of different samples, which manifested that slit-like pores were existed in both $\text{g-C}_3\text{N}_4$ and $\text{g-C}_3\text{N}_4/\text{Ag}_2\text{CrO}_4$ composites [44]. Besides, the corresponding pore size distributions (inset of Fig. 6) demonstrated that $\text{g-C}_3\text{N}_4$ and all the composites presented a wide pore size distribution mainly ranged from 15 to 60 nm, while Ag_2CrO_4 showed a poor pore distribution. This indicated that abundant mesopores and macropores were coexisting which mainly originated from the inherent mesopores and aggregation of plate-like sheets of porous $\text{g-C}_3\text{N}_4$ as shown in SEM and TEM. The Brunauer–Emmett–Teller (BET) surface areas of $\text{g-C}_3\text{N}_4$, ACO/CN-0.2 , ACO/CN-0.3 , ACO/CN-0.4 , ACO/CN-0.6 and Ag_2CrO_4 were 58.1, 52.2, 51.3, 50.9, 47.1 and $20.5 \text{ m}^2/\text{g}$, the average pore volume were 0.182, 0.179, 0.158, 0.150, 0.124 and 0.022 cc/g, respectively. It was found that the BET surface areas and pore volumes of $\text{g-C}_3\text{N}_4/\text{Ag}_2\text{CrO}_4$ composites reduced with the increased content of Ag_2CrO_4 , especially for ACO/CN-0.6 , which were mainly attributed to the blocking of the pores caused by the excess Ag_2CrO_4 nanoparticles. The appropriate incorporation of Ag_2CrO_4 did not destroy the pore structure of $\text{g-C}_3\text{N}_4$ and had slight effect on its specific surface area. The high BET surface area and pore volume were beneficial to the adsorption of dye molecules and provided more active sites in photocatalytic reactions.

Fig. 7 displayed the UV-vis diffuse reflectance spectra of the $\text{g-C}_3\text{N}_4/\text{Ag}_2\text{CrO}_4$ composite photocatalysts with different mass ratio of Ag_2CrO_4 , along with pure $\text{g-C}_3\text{N}_4$ and Ag_2CrO_4 . As we can see, pure $\text{g-C}_3\text{N}_4$ showed an absorption edge at about 450 nm, whereas pure Ag_2CrO_4 had a broad absorption in the whole visible region. For $\text{g-C}_3\text{N}_4/\text{Ag}_2\text{CrO}_4$ composites, two distinct absorption steps were appeared in the spectra, implying the composite pho-

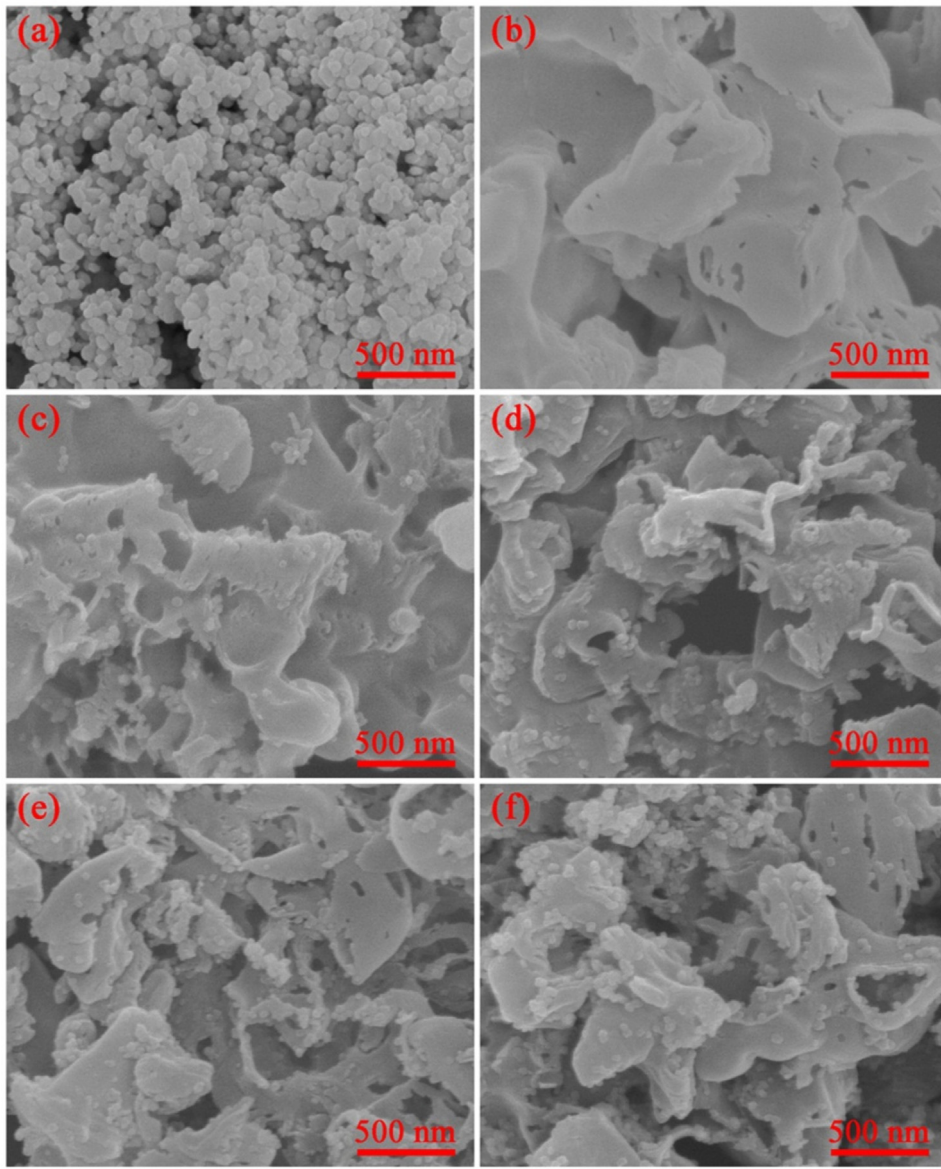


Fig. 4. SEM images of as-prepared photocatalysts: (a) Ag_2CrO_4 nanoparticles, (b) $\text{g-C}_3\text{N}_4$, (c) ACO/CN-0.2, (d) ACO/CN-0.3, (e) ACO/CN-0.4, (f) ACO/CN-0.6.

tocatalysts exhibited both optical absorption properties of $\text{g-C}_3\text{N}_4$ and Ag_2CrO_4 [45,46]. As the increased content of Ag_2CrO_4 , the absorption in visible region was stepwise strengthened and the absorption edge shifted toward the Ag_2CrO_4 gradually, demonstrating that Ag_2CrO_4 was beneficial to the visible-light absorption of $\text{g-C}_3\text{N}_4/\text{Ag}_2\text{CrO}_4$ composites. The band gaps of the photocatalysts were calculated by Kubelka–Munk (KM) transformation [47]:

$$\alpha h\nu = A(h\nu - E_g)^{n/2} \quad (1)$$

where α , h , ν , A and E_g are absorption coefficient, Planck constant, light frequency, a constant and band gap energy, respectively. The value of n is decided by the property of the semiconductor, Ag_2CrO_4 is an indirect band gap semiconductor, the value of n is 4 [15,19]; $\text{g-C}_3\text{N}_4$ is a direct band gap semiconductor and the value is 1 [47,48]. The calculation results were presented in Fig. 7b and 7c, the band gap of $\text{g-C}_3\text{N}_4$ was 2.9 eV and for Ag_2CrO_4 was 1.72 eV. Furthermore, the conduction band potential (E_{CB}) and valance band potential

(E_{VB}) of the semiconductor were determined by the empirical equation [49]:

$$E_{VB} = \chi - E^e + 0.5E_g \quad (2)$$

$$E_{CB} = E_{VB} - E_g \quad (3)$$

where χ is the absolute electronegativity of the semiconductor. For $\text{g-C}_3\text{N}_4$ and Ag_2CrO_4 , the values of χ are 4.73 and 5.86 eV, respectively [18,49]. E^e is the energy of free electrons with the hydrogen scale (about 4.5 eV). Thus, the E_{VB} potentials of $\text{g-C}_3\text{N}_4$ and Ag_2CrO_4 were 1.68 and 2.22 eV, the E_{CB} potentials were –1.22 and 0.50 eV, respectively. (vs. NHE)

3.2. Photocatalytic activity and stability

The photocatalytic activities of as-prepared photocatalysts were investigated through degrading RhB and MB aqueous solution under visible-light irradiation. As illustrated in Fig. 8, self-degradation of RhB and MB was negligible without addition of photocatalysts, indicating these two types of organic dyes were photochemical stable. Pure Ag_2CrO_4 and $\text{g-C}_3\text{N}_4$ showed unsat-

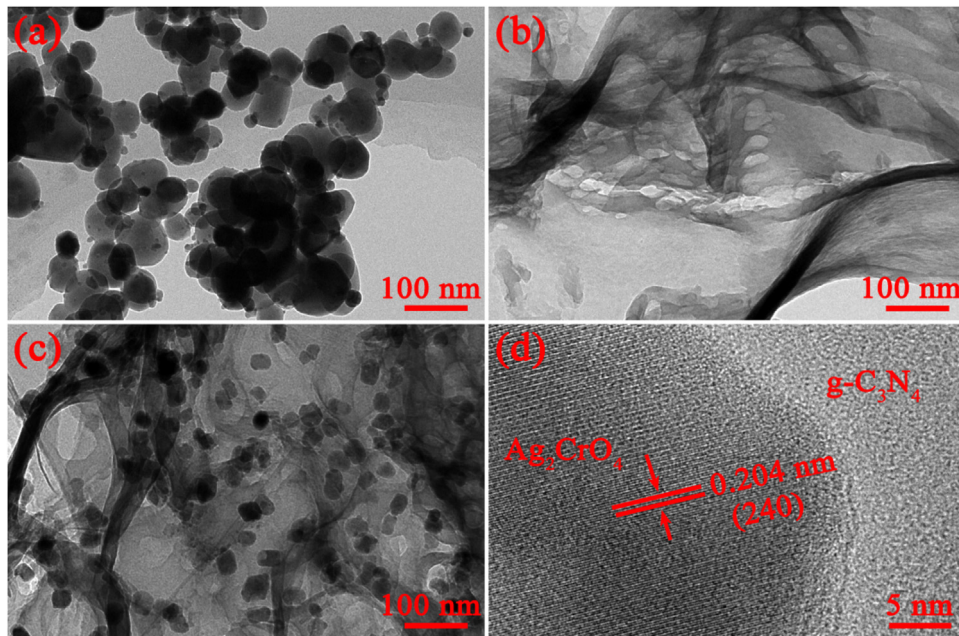


Fig. 5. TEM images of (a) Ag_2CrO_4 , (b) $\text{g-C}_3\text{N}_4$, (c) ACO/CN-0.3 and (d) HRTEM of ACO/CN-0.3.

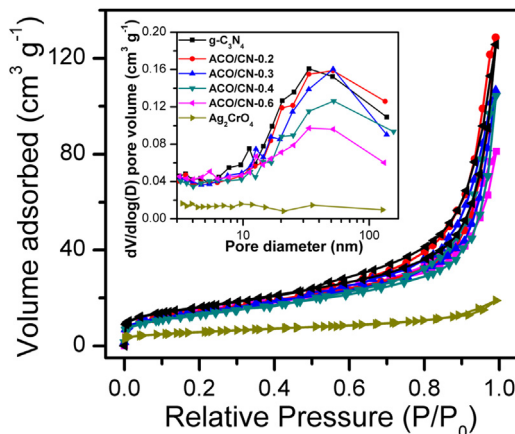


Fig. 6. N_2 adsorption-desorption isotherms and corresponding pore diameter distribution curves (inset) of Ag_2CrO_4 , $\text{g-C}_3\text{N}_4$, and $\text{g-C}_3\text{N}_4/\text{Ag}_2\text{CrO}_4$ composites.

isfactory activities mainly due to their fast recombination rate of photo-generated charge carriers and the serious agglomeration of Ag_2CrO_4 nanoparticles. All the composites showed remarkably enhanced phototocatalytic activities under same experimental condition. As the content of Ag_2CrO_4 decreased, the photocatalytic activities of the $\text{g-C}_3\text{N}_4/\text{Ag}_2\text{CrO}_4$ composites were improved gradually and then decreased. ACO/CN-0.3 exhibited the highest activity in degrading both RhB and MB, about 99.2% and 99.1% of RhB and MB were removed after 90 and 120 min visible-light irradiation, respectively. As we all known, the mass ratio of components has a great influence on the photocatalytic performance in heterogeneous photocatalyst system [27,37,50]. An appropriate amount of Ag_2CrO_4 in the composites not only broadened the absorption in visible light region, but also had a synergistic effect with $\text{g-C}_3\text{N}_4$ which was beneficial to the fast separation of photo-generated charge carriers and thus enhanced the photocatalytic activity. Conversely, excessive loading of Ag_2CrO_4 was easy to reunite and hindered the light absorption of $\text{g-C}_3\text{N}_4$, restricting the improvement of photocatalytic activity. The photodegrada-

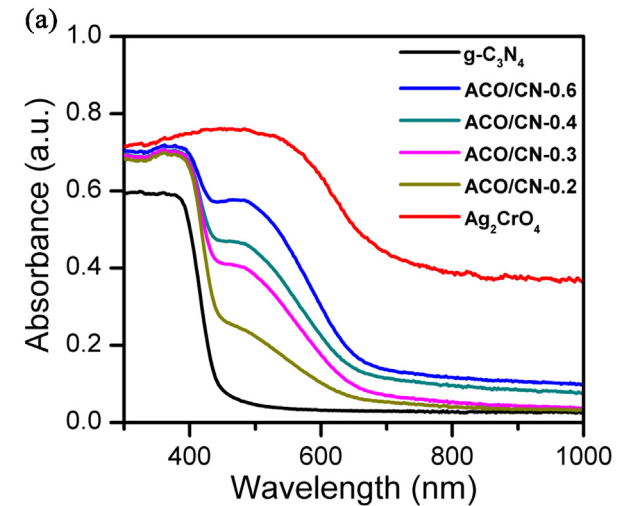


Fig. 7. (a) UV-vis diffuse reflectance spectra of Ag_2CrO_4 , $\text{g-C}_3\text{N}_4$, and $\text{g-C}_3\text{N}_4/\text{Ag}_2\text{CrO}_4$ composites with different mass ratio, (b) the plots of the $(\text{Ahv})^2$ vs (hv) for $\text{g-C}_3\text{N}_4$, (c) the plots of the $(\text{Ahv})^{1/2}$ vs (hv) for Ag_2CrO_4 .

tion kinetic constants of different samples were described as the pseudo-first-order equation as follow:

$$\ln(C_0/C) = kt \quad (4)$$

where k is the apparent kinetic rate constants, t is successive irradiation time, C and C_0 are the real-time concentration at t and the initial concentration of the organic dyes, respectively. As illustrated

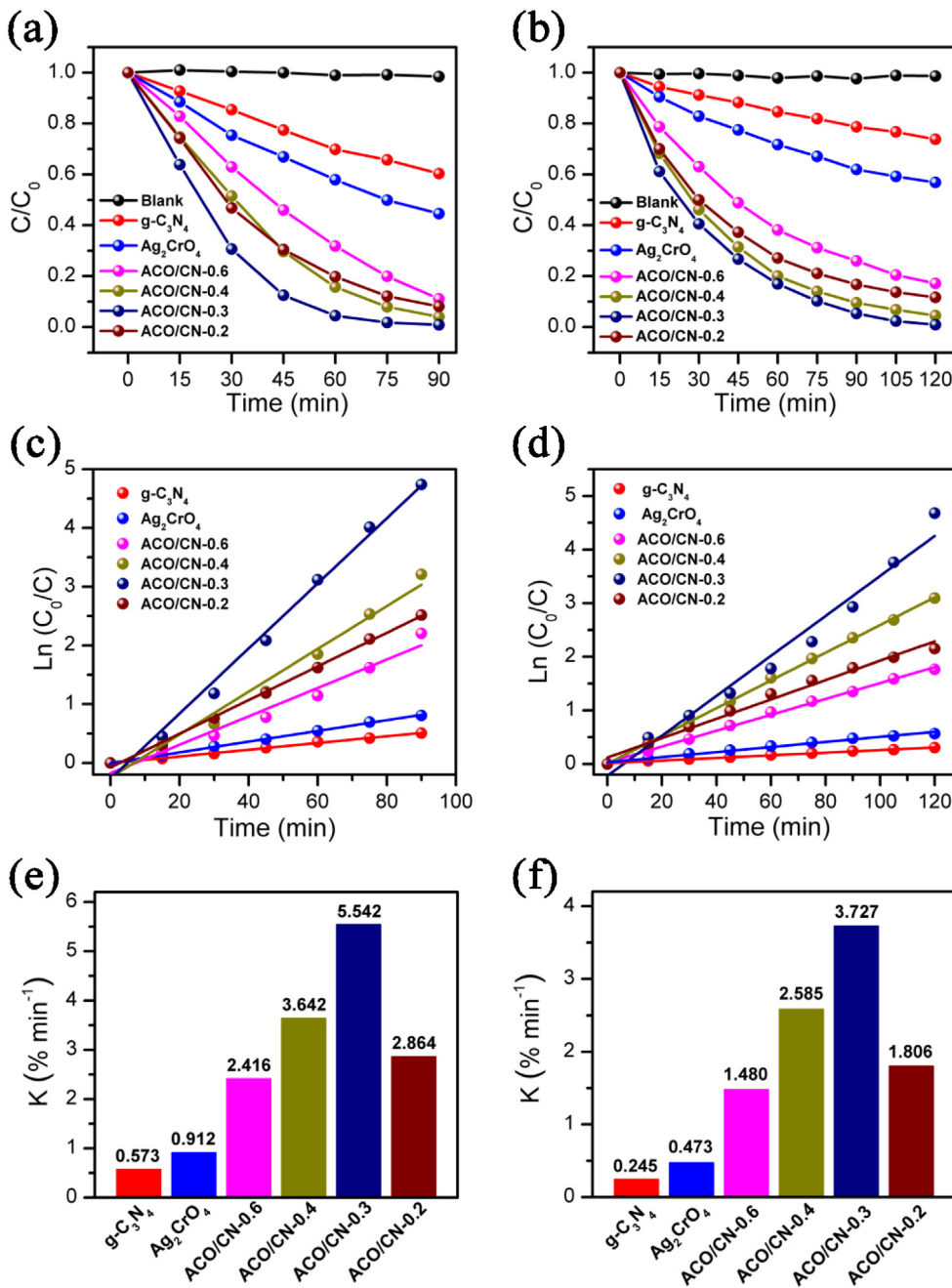


Fig. 8. Photodegradation rate of RhB (a) and MB (b) over all samples under visible light irradiation, the $\ln(C_0/C)$ as a function of irradiation time for RhB (c) and MB (d) degradation, the apparent rate constants over all samples for degradation of RhB (e) and MB (f).

in Fig. 8c–f, the values of k were determined from the slopes of $\ln(C_0/C)$ versus t . Obviously, ACO/CN-0.3 displayed the fastest reaction rate in both degradation of RhB and MB with the apparent rate constants of 5.542 and 3.727 min^{-1} , respectively. The k values of all the composites were enormously higher than those of bare Ag_2CrO_4 and $\text{g-C}_3\text{N}_4$.

The renewable stability is an important index for practicality of the photocatalysts. Therefore, the repeated photocatalytic experiments were implemented to evaluate the photocatalytic cycle stability of the photocatalysts. Briefly, the used ACO/CN-0.3 was collected via high-speed centrifugation, washed and dried. The again collected sample (10 mg) was applied in RhB (10 mg/L) degradation under the same experimental conditions. From Fig. 9, the photocatalytic activity of pure Ag_2CrO_4 showed a significant decline in cycling test due to the photocorrosion under visible

light irradiation, while no obvious decrease for ACO/CN-0.3 after four successive cycling reactions. ACO/CN-0.3 remained 97.1% of degradation rate in the fourth cycling experiment within 90 min, showing only 2.1% attenuation compared with the first experiment, demonstrating the $\text{g-C}_3\text{N}_4/\text{Ag}_2\text{CrO}_4$ composite photocatalysts had a favorable reusability.

To investigate the morphology and structure stabilities, SEM and XRD of the reused photocatalysts were carried out. It could be clearly seen in Fig. 10a and b that the morphology was relatively stable and the Ag_2CrO_4 particles still tightly attached on the surface of $\text{g-C}_3\text{N}_4$. From XRD patterns presented in Fig. 10c, the reused ACO/CN-0.3 remained the same crystalline structure with the fresh sample and no new diffraction peaks appeared in the patterns, revealing the composite photocatalysts showed high structure stability. While for reused Ag_2CrO_4 , a new peak appeared at $2\theta = 38.1^\circ$.

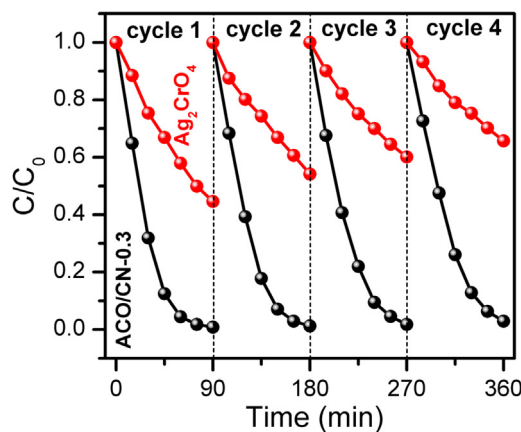


Fig. 9. Recyclability of the ACO/CN-0.3 and Ag₂CrO₄ in four successive experiments for degradation of RhB under visible light irradiation.

and another strengthened at 44.3° were corresponding to the silver (JCPDS No. 04-0783), that meant pure Ag₂CrO₄ was partly decomposed during photocatalytic reactions. The results indicated that the g-C₃N₄/Ag₂CrO₄ hybrid showed the excellent photochemical stability.

In order to further study the reason of enhanced photochemical stability, the Ag 3d HRXPS spectra of ACO/CN-0.3 and Ag₂CrO₄ before and after successive reactions were performed. As shown in Fig. 11, ACO/CN-0.3 exhibited two peaks at 368.1 and 374.1 eV were ascribed to Ag⁺ as mentioned above, whereas two weak peaks appeared in the reused sample were ascribed to Ag⁰, indicating a small fraction of Ag₂CrO₄ was reduced to Ag⁰ even though the g-C₃N₄/Ag₂CrO₄ composites possessed a high stability. The calculated molar ratio of surface Ag⁰ to Ag⁺ was about 4.9% which was

too low to be detected by XRD and no Ag⁰ was detected in the fresh ACO/CN-0.3. Differing from ACO/CN-0.3, the reused Ag₂CrO₄ exhibited two distinct peaks related to Ag⁰, which was about 26.5% of surface Ag⁰ to Ag⁺, 23% more than fresh sample (3.5%), suggesting that bare Ag₂CrO₄ was unstable under visible-light irradiation, easily to be decomposed to Ag⁰. These results further confirmed that g-C₃N₄ indeed acted as an electron acceptor and provided a pathway for accelerated separation of photo-generated electron-hole pairs thus inhibited the photocorrosion of Ag₂CrO₄, resulting in the increased stability of Ag₂CrO₄ and enhanced photocatalytic activity.

3.3. Photocatalytic mechanism

To study the photocatalytic mechanism in depth, active species trapping experiments were carried out to investigate the contributing active species during the reaction process. Ethylenediamine tetraacetic acid disodium salt (EDTA-2Na, 5 mM), *p*-benzoquinone (BZQ, 5 mM) and *tert*-butyl alcohol (TBA 10 mM) were employed as the scavengers for photo-generated holes (h⁺), superoxide radical (•O₂[−]) and hydroxyl radical (•OH), respectively. The experiments were performed in degradation of RhB and MB under same conditions as above. Fig. 12 clearly illustrated the experimental results, the degradation rates of RhB and MB were distinctly suppressed with the additions of EDTA-2Na and BZQ, implying the h⁺ and •O₂[−] were the main active species in the photocatalytic process. However, the degradation rates were not obviously influenced with the existence of TBA, only a slight decline was observed, suggesting •OH played an insignificant contribution in the photocatalytic reaction.

PL is a widely used technique to investigate the migration and recombination process of the photo-generated electron-hole pairs. According to the reported literatures [51,52], the intensity of PL demonstrated the recombination rate of the electron-hole

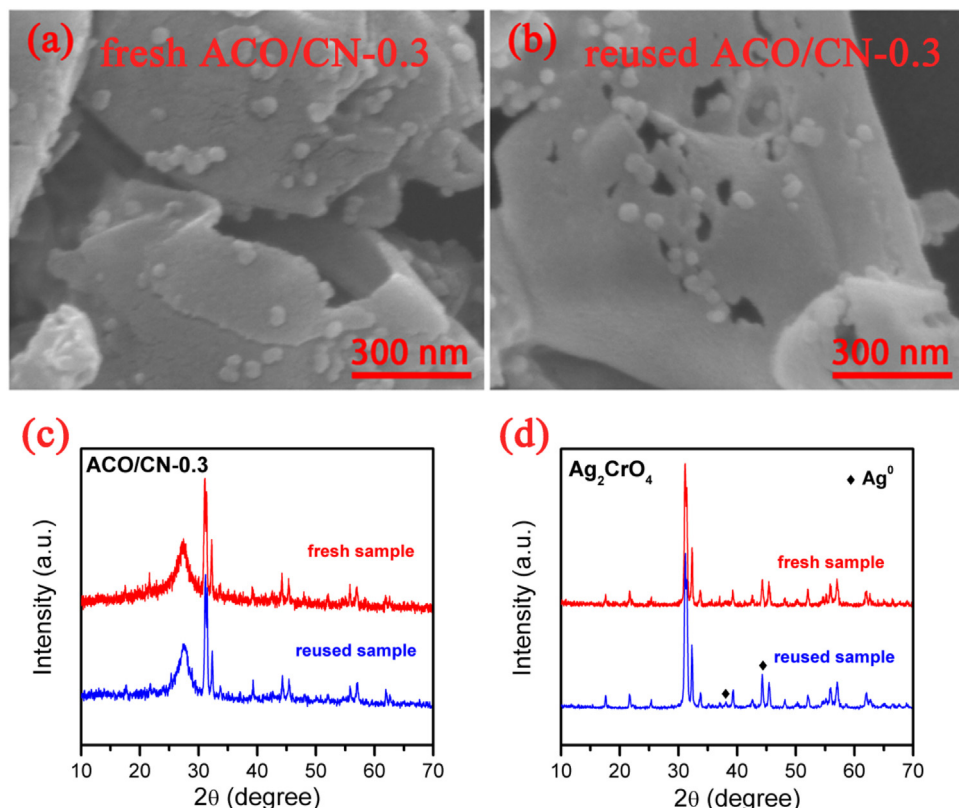


Fig. 10. SEM images of (a) fresh ACO/CN-0.3 and (b) reused ACO/CN-0.3; XRD patterns of (c) fresh and reused ACO/CN-0.3, (d) fresh and reused Ag₂CrO₄.

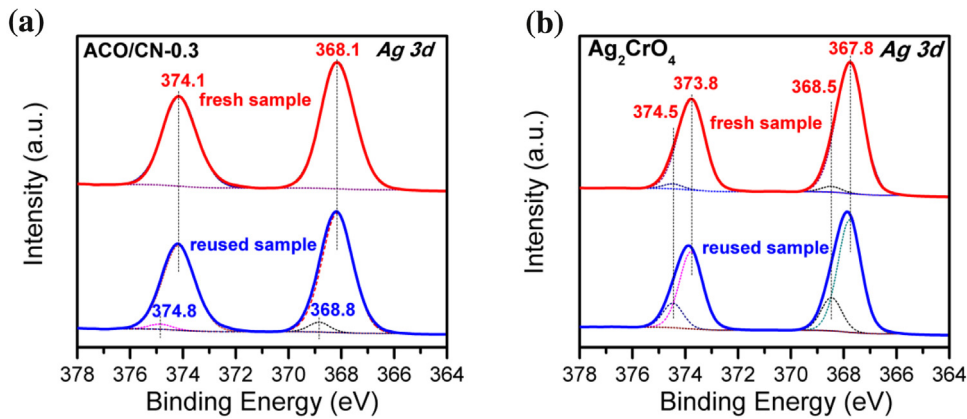


Fig. 11. Ag 3d HRXPS spectra of (a) fresh and reused ACO/CN-0.3, (b) fresh and reused Ag₂CrO₄.

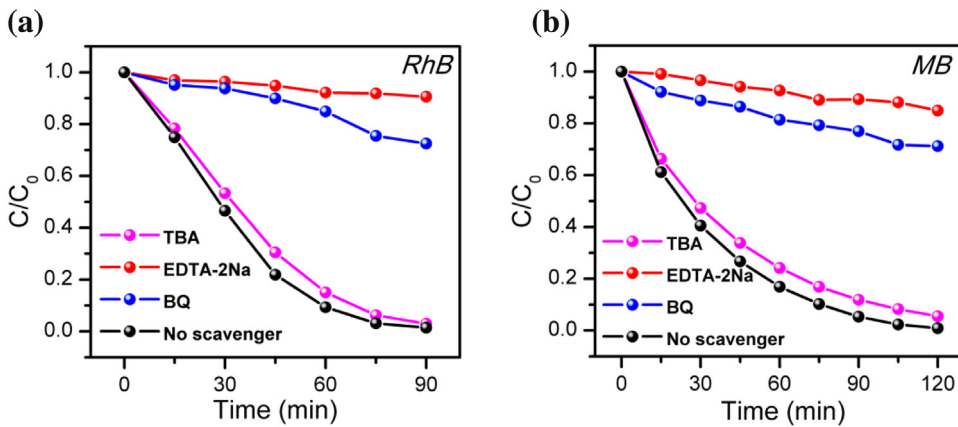


Fig. 12. Active species trapping experiments of ACO/CN-0.3 in degrading (a) RhB and (b) MB.

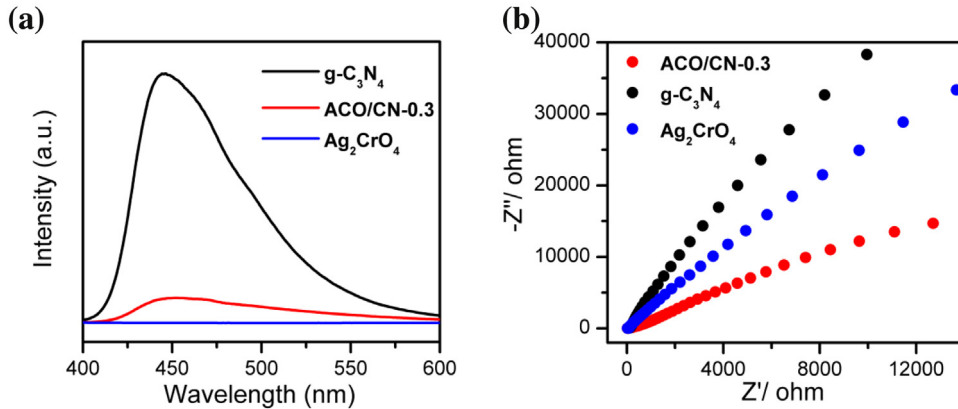


Fig. 13. (a) Photoluminescence spectra (PL) of g-C₃N₄, Ag₂CrO₄ and ACO/CN-0.3 with an excitation wavelength of 370 nm; (b) Electrochemical impedance spectroscopy (EIS) Nyquist plots of g-C₃N₄, Ag₂CrO₄ and ACO/CN-0.3.

pairs. In this experiment, PL spectra of g-C₃N₄, Ag₂CrO₄ and ACO/CN-0.3 were measured under 370 nm excitation wavelength at room temperature. As presented in Fig. 13a, pure Ag₂CrO₄ didn't show distinct photoluminescence property, g-C₃N₄ exhibited a strong and broad peak at around 445 nm under 370 nm excitation wavelength, which suggested the fast recombination rate of its photo-induced carriers. By contrast, ACO/CN-0.3 exhibited a much lower PL intensity, implying that the recombination of electron-hole pairs was significantly inhibited after hybrid. Furthermore, the same result was also proved by EIS shown in Fig. 13b, compared with g-C₃N₄ and Ag₂CrO₄, the much smaller radius of

curvature on the EIS Nyquist plot implied that ACO/CN-0.3 exhibited a decreased interfacial charge transfer resistance, indicating a remarkably enhanced efficiency in separation of photo-generated charge carriers [53,54].

Based on the above experimental results, the plausible photocatalytic mechanism was discussed detailedly. When the g-C₃N₄/Ag₂CrO₄ composites were exposed under visible light, both Ag₂CrO₄ and g-C₃N₄ could be excited and yield electron-hole pairs. According to the double charge transfer theory [21], the photo-generated electrons of g-C₃N₄ would migrate to the CB of Ag₂CrO₄ and the holes of Ag₂CrO₄ would transfer to the

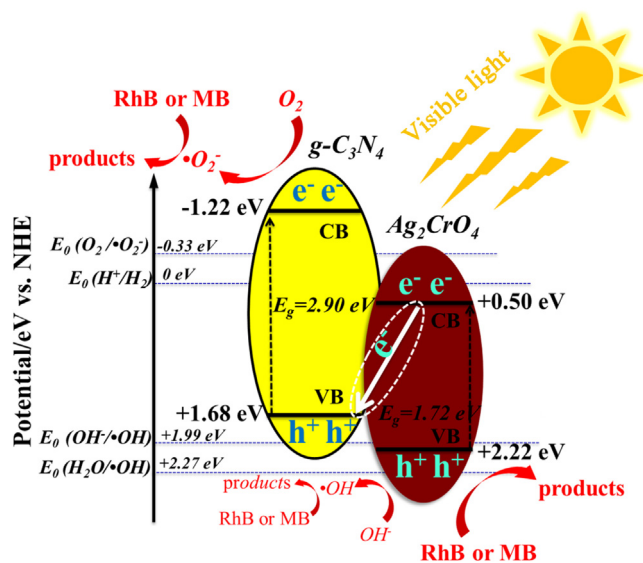
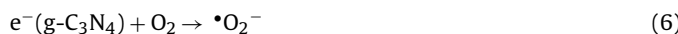
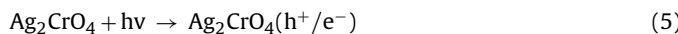


Fig. 14. Z-scheme mechanism for porous $\text{g-C}_3\text{N}_4/\text{Ag}_2\text{CrO}_4$ composite photocatalysts.

VB of $\text{g-C}_3\text{N}_4$ because the VB and CB potentials of Ag_2CrO_4 were both lower than those of $\text{g-C}_3\text{N}_4$. However, if the composites followed the double charge transfer theory, the electrons in the CB of Ag_2CrO_4 could not reduce O_2 to generate $\bullet\text{O}_2^-$ due to the CB potential of Ag_2CrO_4 (-1.22 eV vs. NHE) was higher than $E_0(\text{O}_2/\bullet\text{O}_2^-)$ (-0.33 eV vs. NHE), similarly, the holes in VB of $\text{g-C}_3\text{N}_4$ (1.68 eV vs. NHE) could not oxidize OH^- to yield $\bullet\text{OH}$ ($E_0(\text{OH}^-/\bullet\text{OH}) = 1.99 \text{ eV}$ vs. NHE). Actually, though $\bullet\text{OH}$ had little influence on the photocatalytic reaction, both $\bullet\text{O}_2^-$ and $\bullet\text{OH}$ were active species.

Therefore, a Z-scheme mechanism was proposed based on the above analysis. As illustrated in Fig. 14, the photo-generated electrons on the CB of Ag_2CrO_4 could easily transfer to the VB of $\text{g-C}_3\text{N}_4$ and reacted with the holes of $\text{g-C}_3\text{N}_4$. The electrons left at the CB of $\text{g-C}_3\text{N}_4$ reduced O_2 to yield $\bullet\text{O}_2^-$ which is a powerful oxidant for organic dyes degradation. Holes stored in the VB of Ag_2CrO_4 could directly oxidize the pollutants to harmless products and react with surface hydroxyls (OH^-) to generate tiny amounts of $\bullet\text{OH}$. All the relevant reactions were described as follows:



The Z-scheme mechanism enabled the efficient separation of photo-generated charge carriers as well as a strong redox ability for improved photodegradation efficiency of organic dyes. In addition, trace of Ag^+ was reduced to Ag^0 during the reaction process in the presence of $\text{g-C}_3\text{N}_4/\text{Ag}_2\text{CrO}_4$ composites. On the one hand, Ag^0 could act the bridge that contributed to transferring the photo-generated electrons, but on the other hand, the surface Ag^0 partly prevented Ag_2CrO_4 from absorbing visible light, leading to a slight decline of photocatalytic activity [55].

4. Conclusions

In summary, porous $\text{g-C}_3\text{N}_4/\text{Ag}_2\text{CrO}_4$ composites were successfully synthesized via a facile microemulsion-assisted coprecipitation method. The composite photocatalysts exhibited excellent photocatalytic activity and considerable stability toward organic dyes degradation. The optimum composite with 30 wt% Ag_2CrO_4 showed the best photocatalytic activity, the k values of which were almost 6.1 and 9.7 times higher than bare Ag_2CrO_4 and $\text{g-C}_3\text{N}_4$ in RhB degradation, 7.9 and 15.2 times higher in MB degradation, respectively. The photocatalytic mechanism followed a Z-scheme, which accelerated the separation of photo-generated charge carriers meanwhile imparted high redox ability to the composites. In addition, photocorrosion of Ag_2CrO_4 was distinctly restrained through rapidly migrating photo-generated electrons to $\text{g-C}_3\text{N}_4$. Such a facile strategy may contribute to providing an idea for designing and fabricating other high-efficiency $\text{g-C}_3\text{N}_4$ or Ag_2CrO_4 based photocatalysts for addressing energy and environmental issues.

Acknowledgement

This work is financial support by the National Science Foundation of China (51302325; 11674398), Science Fund for Distinguished Young Scholars of Hunan Province (2015JJ1016), the Hunan Youth Innovation Platform, Program for Shenghua Overseas Talent (90600-903030005; 90600-996010162), and the Project of Innovation-driven Plan in Central South University (2015CXS004).

References

- [1] A. Fujishima, K. Honda, *Nature* 238 (1972) 37–38.
- [2] A. Kubacka, M. Fernández-García, G. Colón, *Chem. Rev.* 112 (2012) 1555–1614.
- [3] D.J. Martin, P.J. Reardon, S.J. Moniz, J. Tang, *J. Am. Chem. Soc.* 136 (2014) 12568–12571.
- [4] X. Chen, S. Shen, L. Guo, S.S. Mao, *Chem. Rev.* 110 (2010) 6503–6570.
- [5] Y. Wang, L. Liu, L. Xu, X. Cao, X. Li, Y. Huang, C. Meng, Z. Wang, W. Zhu, *Nanoscale* 6 (2014) 6790–6797.
- [6] X. Pan, Y. Zhao, S. Liu, C.L. Korzeniewski, S. Wang, Z. Fan, *ACS Appl. Mater. Interfaces* 4 (2012) 3944–3950.
- [7] X. Chen, H. Li, H. Wu, Y. Wu, Y. Shang, J. Pan, X. Xiong, *Mater. Lett.* 172 (2016) 52–55.
- [8] L. Tian, L. Ye, J. Liu, L. Lan, *Catal. Commun.* 17 (2012) 99–103.
- [9] W.-K. Jo, T.S. Natarajan, *Chem. Eng. J.* 281 (2015) 549–565.
- [10] J. Pan, J. Li, Z. Yan, B. Zhou, H. Wu, X. Xiong, *Nanoscale* 5 (2013) 3022–3029.
- [11] Y. Wu, M. Xu, X. Chen, S. Yang, H. Wu, J. Pan, X. Xiong, *Nanoscale* 8 (2015) 440–450.
- [12] H. Katsumata, T. Sakai, T. Suzuki, S. Kaneko, *Ind. Eng. Chem. Res.* 53 (2014) 8018–8025.
- [13] Y. He, L. Zhang, B. Teng, M. Fan, *Environ. Sci. Technol.* 49 (2015) 649–656.
- [14] M. Cao, P. Wang, Y. Ao, C. Wang, J. Hou, J. Qian, *Int. J. Hydrogen Energy* 40 (2015) 1016–1025.
- [15] S. Ouyang, Z. Li, Z. Ouyang, T. Yu, J. Ye, Z. Zou, *J. Phys. Chem. C* 112 (2008) 3134–3141.
- [16] D. Santamaría-Pérez, E. Bandiello, D. Errandonea, J. Ruiz-Fuertes, O. Gomis, J.A. Sans, F.J. Manjón, P. Rodríguez-Hernández, A. Muñoz, *J. Phys. Chem. C* 117 (2013) 12239–12248.
- [17] D. Xu, B. Cheng, J. Zhang, W. Wang, J. Yu, W. Ho, *J. Mater. Chem. A* 3 (2015) 20153–20166.
- [18] J. Zhang, W. Yu, J. Liu, B. Liu, *Appl. Surf. Sci.* 358 (2015) 457–462.
- [19] D. Xu, S. Cao, J. Zhang, B. Cheng, J. Yu, *Beilstein J. Nanotechnol.* 5 (2014) 658–666.
- [20] D. Xu, B. Cheng, S. Cao, J. Yu, *Appl. Catal. B: Environ.* 164 (2015) 380–388.
- [21] L. Shi, L. Liang, F. Wang, M. Liu, J. Sun, *Dalton Trans.* 53 (2016) 269–271.
- [22] Y. Tang, X. Hua, C. Liu, *Phys. Chem. Chem. Phys.* 16 (2014) 25321–25329.
- [23] L. Yu, W. Chen, D. Li, J. Wang, Y. Shao, M. He, P. Wang, X. Zheng, *Appl. Catal. B: Environ.* 164 (2015) 453–461.
- [24] W. Yao, B. Zhang, C. Huang, C. Ma, X. Song, Q. Xua, *J. Mater. Chem. B* 2 (2012) 4050–4055.
- [25] Y. Zheng, J. Liu, J. Liang, M. Jaroniec, S.Z. Qiao, *Energy Environ. Sci.* 5 (2012) 6717–6731.
- [26] Y. Wang, X. Wang, M. Antonietti, *Angew. Chem. Int. Ed.* 51 (2012) 68–89.
- [27] S. Kumar, T. Surendar, A. Baruah, V. Shanker, *J. Mater. Chem. A* 1 (2013) 5333–5340.
- [28] Z. Zhao, Y. Sun, F. Dong, *Nanoscale* 7 (2015) 15–37.

- [29] L. Zhu, D. Huang, J. Ma, D. Wu, M. Yang, S. Komarneni, *Ceram. Int.* 41 (2015) 12509–12513.
- [30] F.-J. Zhang, F.-Z. Xie, S.-F. Zhu, J. Liu, J. Zhang, S.-F. Mei, W. Zhao, *Chem. Eng. J.* 228 (2013) 435–441.
- [31] L. Xiong, T. He, *Chem. Mater.* 18 (2006) 2211–2218.
- [32] Z. Xu, J. Yu, J. Low, M. Jaroniec, *ACS Appl. Mater. Interfaces* 6 (2014) 2111–2117.
- [33] F. Xu, W. Xiao, B. Cheng, J. Yu, *Int. J. Hydrogen Energy* 39 (2014) 15394–15402.
- [34] Y. Min, G. He, Q. Xu, Y. Chen, *J. Mater. Chem. A* 2 (2014) 1294–1301.
- [35] S. Kumar, S.T.B. Kumar, A. Baruah, V. Shanker, *J. Phys. Chem. C* 117 (2013) 26135–26143.
- [36] J.-K. Liu, C.-X. Luo, N.-J. Quan, *J. Nanopart. Res.* 10 (2007) 531–535.
- [37] W.-J. Ong, L.K. Putri, L.-L. Tan, S.-P. Chai, S.-T. Yong, *Appl. Catal. B: Environ.* 180 (2016) 530–543.
- [38] B. Chai, F. Zou, W. Chen, *J. Mater. Res.* 30 (2015) 1128–1136.
- [39] M. Lu, Z. Pei, S. Weng, W. Feng, Z. Fang, Z. Zheng, M. Huang, P. Liu, *Phys. Chem. Chem. Phys.* (2014) 21280–21288.
- [40] S. Zhang, J. Li, X. Wang, Y. Huang, M. Zeng, J. Xu, *J. Mater. Chem. A* 3 (2015) 10119–10126.
- [41] Z. Xu, J. Yu, W. Xiao, *Chem. Eur. J.* 19 (2013) 9592–9598.
- [42] R.P. Bagwe, C. Yang, L.R. Hilliard, W. Tan, *Langmuir* 20 (2004) 8336–8342.
- [43] H. Li, J. Liu, W. Hou, N. Du, R. Zhang, X. Tao, *Appl. Catal. B: Environ.* 160–161 (2014) 89–97.
- [44] R. Hao, G. Wang, H. Tang, L. Sun, C. Xu, D. Han, *Appl. Catal. B: Environ.* 187 (2016) 47–58.
- [45] Z. Zhang, C. Shao, X. Li, C. Wang, M. Zhang, Y. Liu, *ACS Appl. Mater. Interfaces* 2 (2010) 2915–2923.
- [46] Z.a. Huang, Q. Sun, K. Lv, Z. Zhang, M. Li, B. Li, *Appl. Catal. B: Environ.* 164 (2015) 420–427.
- [47] S. Meng, X. Ning, T. Zhang, S.-F. Chen, X. Fu, *Phys. Chem. Chem. Phys.* 17 (2015) 11577–11585.
- [48] X. Wang, J.M. Carlsson, K. Domen, M. Antonietti, *Nat. Mater.* 8 (2009) 76–80.
- [49] S. Chen, Y. Hu, S. Meng, X. Fu, *Appl. Catal. B: Environ.* 150–151 (2014) 564–573.
- [50] X. Chen, B. Zhou, S. Yang, H. Wu, Y. Wu, L. Wu, J. Pan, X. Xiong, *RSC Adv.* 5 (2015) 68953–68963.
- [51] J. Ma, C. Wang, H. He, *Appl. Catal. B: Environ.* 184 (2016) 28–34.
- [52] H. Xu, J. Yan, Y. Xu, Y. Song, H. Li, J. Xia, C. Huang, *Appl. Catal. B: Environ.* 129 (2013) 182–193.
- [53] J. Zhou, M. Zhang, Y. Zhu, *Phys. Chem. Chem. Phys.* 16 (2014) 17627–17633.
- [54] L. Liu, Y. Qi, J. Lu, S. Lin, W. An, Y. Liang, W. Cui, *Appl. Catal. B: Environ.* 183 (2016) 133–141.
- [55] Z. Xiu, H. Bo, Y. Wu, X. Hao, *Appl. Surf. Sci.* 289 (2014) 394–399.